Sensors & Diagnostics

PAPER

View Article Online
View Journal | View Issue

Cite this: *Sens. Diagn.*, 2024, **3**, 1689

A dual state emission luminogen based on the 1,3,3-trimethylindoline and chroman-2,4-dione conjugate for highly selective dual channel detection of cyanide ions†

Snehadrinarayan Khatua, * Sumit Kumar Patra, Monosh Rabha, Deikrisha Lyngdoh Lyngkhoi, Jogat Gogoi and Bhaskar Sen

Dual state emission luminogens (DSEgens) with strong fluorescence in both solution and solid states have extensive potential for numerous applications. Herein, a chroman-2,4-dione and indoline conjugate, **2**, was synthesized for highly selective and sensitive turn-on fluorescent detection of cyanide ions. Compound **2** behaves as a molecular rotor and shows the dual state emission (DSE) phenomenon and multicolour emission. It displays bright fluorescence in both the concentrated solution and the solid-state. The compound is nonfluorescent in dilute solution, and with increasing concentration, it shows aggregation caused red-shifted emission. With increasing concentration, the emission colour changes from green to yellow to orange-red. The C=C bond attached to the indoline moiety is a compelling target for nucleophilic addition. Cyanide ions reacted with the probe which remarkably changed the spectroscopic properties. With the gradual addition of cyanide, the colour of the probe solution was changed from yellow to colorless. The very weakly emissive probe **2** rapidly reacted with CN^- and emitted strongly due to the inhibition of internal charge transfer (ICT) from indoline to chroman-2,4-dione. The DSEgen properties and CN sensing were thoroughly investigated and supported using spectroscopic studies, TDDFT, and single-crystal X-ray diffraction.

Received 10th May 2024,
Accepted 31st July 2024

DOI: 10.1039/d4sd00155a

rsc.li/sensors

Introduction

Organic conjugated fluorogens are widely applied in chemical sensing, bioimaging, and optoelectronics because of their outstanding performances, such as smooth preparation, easy modification, high fluorescence brightness, and tunable spectral properties.[1,2] Most organic fluorogens typically exhibit bright fluorescence in solution due to disaggregation-induced emission (DIE) property. But, owing to aggregation-caused quenching (ACQ) behaviour, they meet great challenges in the solid-state.[3,4] In contrast, the aggregation-induced emission (AIE) phenomenon, reported by Tang and co-workers in 2001, effectively compensates for the ACQ effect, where organic molecules show bright fluorescence in the solid-state due to aggregation.[5] These AIE luminogens are non-emissive in some solvents but highly emissive when forming aggregates.[6,7] Therefore, AIEgens and DIEgens both have sharply opposite emission behaviours upon aggregation, and they can only exhibit bright fluorescence in a single state, such as in solution or in the solid-state.[8–11]

Of late, researchers have developed dual-state emission luminogens (DSEgens) with strong fluorescence in both solution and the solid state, which filled the gap between AIEgens and DIEgens (Chart S1 in the ESI†). For the wide application of DSEgens in both solution and the solid-state, issues associated with ACQ and AIE materials should be overcome by the exploration of DSEgens.[12–16] Among valid design strategies for organic DSEgens, one essential approach is to add conjugation-induced rigidity in twisted molecules, which facilitates the emission in solution by suppressing intramolecular rotation and vibration since fluorescence quenching in the solid-state, which is caused by π–π stacking, is avoided by twisted structure formation.[17–21] DSEgens can also be attained by incorporating bulk substituents into molecular structures to forbid π–π stacking in the solid-state.[22,23] The third design strategy for DSEgens is a zero-twist donor–acceptor molecule that was also found as a dual-state emitter. A recent study showed that D–π–A structures

Centre for Advanced Studies, Department of Chemistry, North-Eastern Hill University, Shillong, Meghalaya 793022, India. E-mail: snehadri@gmail.com, skhatua@nehu.ac.in

† Electronic supplementary information (ESI) available: Experimental details, spectral data, crystallographic and computational study. CCDC 2085904, 2085905 and 2373472. For ESI and crystallographic data in CIF or other electronic format see DOI: **https://doi.org/10.1039/d4sd00155a**

can also be used to achieve DSEgen properties.[24–28] Despite considerable efforts to develop novel organic fluorogens, highly luminescent DSEgen materials are still underexplored due to their imprecise luminescence mechanism.[29–33] Therefore, diligent study and guidance are still desirable to construct DSEgens with highly efficacious fluorescence properties for valuable application.[34–39]

Cyanide is one of the most hazardous chemicals both in biology and the environment due to its extremely high toxicity to mammals.[40,41] According to the World Health Organization (WHO), the maximum permissive level of cyanide in drinking water is 1.9 μM.[42,43] However, it is widely utilized in chemical and industrial processes, for instance, synthetic fertilizers, synthetic fibers, pharmaceuticals, plastic manufacturing, electroplating, metallurgy, and the gold-extraction process.[44–48] Hence, there is a significant concern in developing sensitive and selective detection methods for cyanide ions.[49–53] Fluorescent and/or colorimetric cyanide probes are highly attractive for simple operation, versatile adaptation, low cost, portability, excellent sensitivity, and rapid response.[54–58] Among the variety of signal transductions, internal charge transfer (ICT) has been successfully utilized as a tool of choice in fluorescent sensor design for various analytes.[59–64] These sensors comprise a donor–acceptor moiety, where the fluorescence emission is enhanced upon analyte interaction due to inhibition of ICT.[65,66]

Herein, we report a 1,3,3-trimethylindoline and chroman-2,4-dione conjugate, **2** (Scheme 1), as a highly selective and sensitive colorimetric and fluorometric cyanide probe. Compound **2** shows a dual-state emission phenomenon and shows bright fluorescence in both the concentrated solution as well as in the solid-state. Furthermore, with increasing concentration in the solution phase, it shows aggregation caused red-shifted emission. The red-shifted and multicolour emission is due to the aggregation in solution and the solid state, which is supported by theoretical calculation and single crystal structure. The integration of the chroman-2,4-dione into the indoline induced the internal charge transfer (ICT) process. The C=C bond attached to the chroman-2,4-dione (Scheme 1) is an effective target for the nucleophilic addition of cyanide, inducing a remarkable change in spectroscopic properties. With the gradual addition of cyanide, the colour of the solution changed from yellow to colourless and the very weakly emissive probe **2** rapidly reacted with CN^- and emitted strongly due to the inhibition of internal charge transfer (ICT).

Results and discussion

Synthesis and characterization

Compound **2** was synthesized in two steps. At first, 4-chloro-3-formylcoumarin (**1**) was prepared from 4-hydroxycoumarin using $POCl_3$ in DMF and isolated in high yield (78%) (Scheme 2). Probe **2** was obtained by stirring **1** with 1,2,3,3-tetramethyl-3*H*-indolium iodide in EtOH at 90 °C and isolated as a dark red solid in 74% yield (Scheme 2). Compounds **1** and **2** were characterized by ^{1}H NMR, ^{13}C NMR, ^{1}H–^{1}H COSY spectroscopy, and ESI-HRMS spectrometry (Fig. S1–S7 in the ESI†). The solid-state structure of **1** and **2** was determined by single-crystal X-ray diffraction (Fig. 2). NMR spectra of **1** and **2**, recorded in $CDCl_3$ at room temperature, clearly show all expected peaks. The HRMS spectra of **1** and **2** exhibit peaks at m/z = 208.9984 (calcd. 208.9927) and 346.1399 (calcd. 346.1365), respectively, assigned to singly positively charged species.

The ^{1}H NMR spectrum of compound **2** exhibits two sets of mutually related signals, whereas, in the crystal structures (*vide infra*) both the isomers (*Z* and *E*) of compound **2** are observed. Initially, we expected that the possibility of a *trans*- or *cis*-form could be a reason for this observation. However, the *trans*- and *cis*-isomers of the probe should be dissimilar obviously by spin–spin coupling constants of the *trans*- and *cis*-protons H_a and H_b. However, no difference is observed in the spectra of compound **2**, and both the groups of doublets have the same coupling constants, for instance, J = 14.8 Hz for two $H_{6,7}$ protons (Fig. 1). The most agreeable explanation for the two sets of signals in NMR spectroscopy of probe **2** is the possibility of existing in two different configurations (Scheme 2). Herein, both configurations have similar spin–spin coupling constants of the H(6)–H(7) protons (in each of the structures shown, they are in the *trans*-position toward

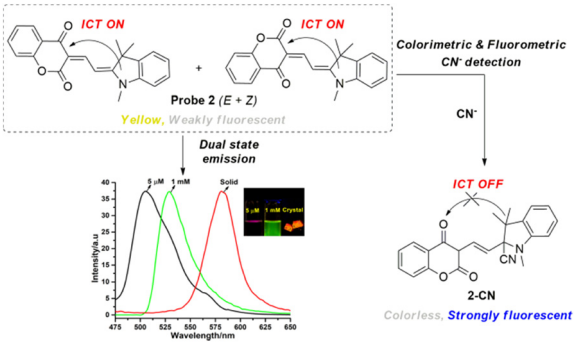

Scheme 1 Schematic illustration showing dual state emission (DSE) property and cyanide detection by probe **2**.

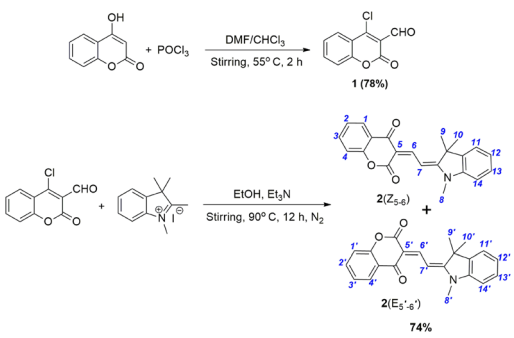

Scheme 2 Synthetic scheme of 4-chloro-3-formylcoumarin (**1**) and compound **2**.

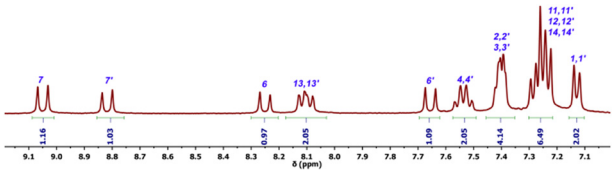

Fig. 1 Partial ^{1}H NMR spectrum of **2** in $CDCl_3$.

each other) and differ insignificantly by the calculated values of the standard energies of formation. Traven *et al.* first reported a similar type of isomer.[67] They did ^{1}H-NMR of the isomer at different solvents ($CDCl_3$, DMSO-d_6, and $CDCl_3$-DMSO-d_6 (1 : 1) mixture) at different temperatures (293, 303, 313, and 323 K) to differentiate the two isomers. But, the character of the ^{1}H NMR spectrum of the isomers undergoes no substantial changes. They concluded that in these types of isomers, both configurations are the most stable and have similar ΔH_f values, which cannot be distinguished by NMR spectra.

Crystal structure of compounds 1 and 2

Diffraction quality, yellow plate-type single crystals of compound **1** were obtained from acetone after 4 days. The compound was crystallized in the triclinic $P\bar{1}$ space group. The structure of the compound is depicted in Fig. 2A. The asymmetric unit contains two independent molecules of **1**. Compound **1** contains both oxygen and chlorine atoms. It forms C–Cl···O halogen bonding and C–H···O hydrogen bonding interaction with neighbouring units and forms an extended two-dimensional (2D) network, which is shown in Fig. 2B. Diffraction quality reddish plate-type single crystals of the *Z*-isomer of compound **2** were obtained from $CHCl_3$/MeOH after three days. The *Z*-isomer of **2** crystallized in the triclinic $P\bar{1}$ space group. The structure of the compound is depicted in Fig. 2C. After several trials, we were able to get the crystal of the *E*-isomer of compound **2** from $CHCl_3$/MeOH after one week. It crystallized in the monoclinic $C2/m$ space group (Fig. 2D). Here, an extended 2D supramolecular network is formed due to the C–H···π and C–H···O hydrogen bonding interaction between the neighbouring units (Fig. 2E). The details of crystal data collection and refinement for **1** and **2** are given in Table S1.†

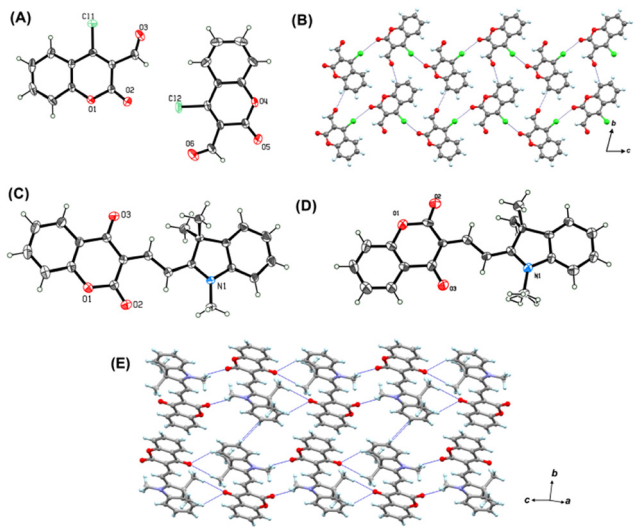

Fig. 2 (A) ORTEP of **1** (CCDC-2085904) with 30% thermal ellipsoid probability. (B) View of the 2D packing diagram of **1** along the crystallographic *a*-axis. ORTEP of (C) *Z*-isomer of **2** (CCDC-2085905) and (D) *E*-isomer of **2** (CCDC-2373472) with 30% thermal ellipsoid probability. (E) View of the 2D packing diagram of the *Z*-isomer of **2** along the crystallographic *b*-axis.

Dual state emission behaviour in compound 2

AIEgens and ACQgens have sharply opposite emission behaviours upon aggregation, and both can exhibit bright luminescence only in a single state *i.e.* solution or the solid state. Recently, there has been an increasing interest in dual-state emission luminogens (DSEgens) because they intensely emit in both the solution and solid state. However, there is no suitable design strategy for obtaining DSEgens, and the modification of luminescent molecules with spacers like alkyl chains can effectively prohibit the π–π stacking in the solid state, diminishing the ACQ effect. Compound **2** emits very weakly in dilute CH_3CN solution (5 μM) and bright-green emission is observed in highly concentrated solution (10 000 μM). Meanwhile in the solid state, it exhibits intense orange-red fluorescence under UV-light illumination. Fig. 3A shows that the emission maximum (λ_{em}) of probe **2** in CH_3CN (5 μM) is located at 503 nm, while it is red shifted to 515 nm (50 μM), 518 nm (100 μM), 526 nm (500 μM), 528 nm (1000 μM), 540 nm (1000 μM) and finally 580 nm in the solid state. The red shift in the emission maxima may be due to the intermolecular interactions between the molecules in the solid state. Surprisingly, it also helps in realizing the unique aggregation caused red-shifted emission effect with increasing the probe concentration in solution. The fluorescence emission wavelength (λ_{em}) was red-shifted from 503 to 540 nm when the concentration of probe **2** was

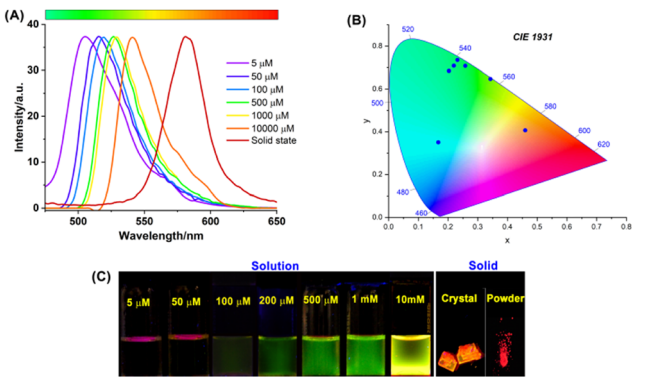

Fig. 3 (A) Normalized fluorescence spectra of **2** at different concentration (5.0 μM to 10 mM) in CH_3CN and in the solid state (λ_{ex} = 485 nm). (B) CIE plot (C) digital photographs of CH_3CN solution of probe **2** at different concentrations (5.0 μM to 10 mM) in CH_3CN and solid powder, and crystal, showing multicolor fluorescence under UV light illumination (365 nm).

increased from 5 μM to 10 000 μM (Fig. 3A). The CIE diagram of the probe in the different concentrations as well as in the solid state shows a variation of luminescence color with increasing concentration (Fig. 3B). Red shifting of the spectra occurs, which is highest in the solid state. The colours, as indicated in Fig. 3B, show that 50–1000 μM of the compound emits colour in the same region with almost the same intensity. The solid-state of the compound has an orange-coloured emission with the highest wavelength. Digital photographs of probe **2** in acetonitrile solution at different concentrations and the solid state show multicolour fluorescence under UV light illumination (Fig. 3C). The probe, due to the efficient aggregation, restricts the intramolecular rotation at a higher concentration, resulting in red shifted emission due to the formation of nano aggregates *via* intermolecular self-assembly. Further, we investigated the solvent-dependent fluorescence using an acetonitrile/PEG gradient to determine whether the restriction of intramolecular rotation (RIR) in probe **2** will enhance its fluorescence. As expected, the fluorescence intensity is concomitantly enhanced with increasing solvent viscosity due to the restriction of intramolecular rotation around the C9–C10 bond in probe **2**. The probe shows ~9-fold fluorescence enhancement at 503 nm at 95% PEG in acetonitrile (Fig. 4A). Further the bathochromic shift of the absorption band at a higher fraction of PEG could be attributed to *J*-aggregate formation in the aggregated state (Fig. 4B). The zigzag 1D chain and 2D crystal packing also support the formation of *J*-aggregates in the solid state (Fig. 2D). In addition, the TCSPC experiment shows that the lifetime of **2** in acetonitrile exhibits a lower fluorescence lifetime (τ) of 0.1076 ns. In contrast, in 90% PEG solution, it shows a higher fluorescence lifetime (τ = 1.23 ns) (Fig. 4C). Moreover, the UV-vis spectral baseline of **2** (CH_3CN, 10 μM) is shifted with increasing amount of PEG (0–95%), which is attributed to the scattering

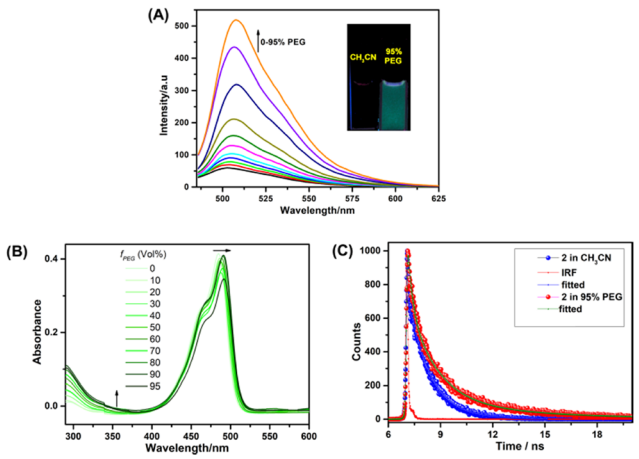

Fig. 4 (A) Fluorescence spectra of **2** (5.0 μM) with increasing amount of PEG (0–95%) in CH_3CN (λ_{ex} = 485 nm). (Inset) Digital photographs of **2** in CH_3CN and in 95% PEG under UV light (365 nm). (B) UV-vis spectra of **2** (5 μM) with increasing amount of PEG (0–95%) in CH_3CN. (C) Time-resolved fluorescence spectra of **2** in CH_3CN and 95% PEG solution.

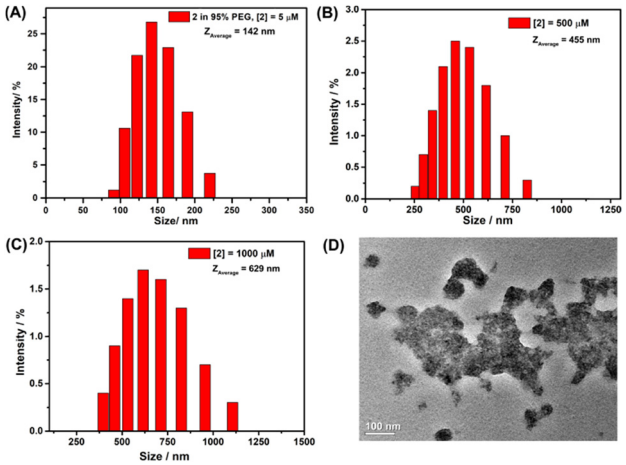

Fig. 5 Particle size distribution of **2** in the CH_3CN–PEG (5 : 95; v/v) mixture at (A) 5 μM, (B) 5 mM and (C) 10 mM concentration. (D) TEM image of **2** (5 μM) in the CH_3CN–PEG mixture (5 : 95; v/v).

of light by the aggregated particles in solution (Fig. 4B). The formation of aggregated particles of **2** in high concentration and viscous medium was confirmed by a dynamic light scattering (DLS) experiment. The hydrodynamic diameters of the aggregated particles of probe **2** at f_{PEG} = 95% range from 80 to 230 nm, with a $Z_{average}$ of 142 nm (Fig. 5A). Similarly, the particle size of probe **2** at 5 mM and 10 mM acetonitrile are in the range of 250 to 800 nm with a $Z_{average}$ of 455 nm (Fig. 5B) and 400 to 1200 nm with a $Z_{average}$ of 629 nm (Fig. 5C) respectively. Further, the TEM images of **2** in dense medium (f_{PEG} = 95%) are consistent with the DLS results, supporting the formation of nano-aggregates (Fig. 5D). The energy levels of the HOMO and LUMO of **2** were compared in the solution state (monomer form) and solid state (dimeric form) to get an insight into the electronic structures. In the solid state, the energy of the LUMO is significantly decreased, whereas the energy of the HOMO is increased slightly compared to the solution state. However, the HOMO to LUMO energy gap (ΔE = 2.9 eV) in the solid state is lowered significantly compared with the solution state (ΔE = 3.27 eV), which leads to the red-shifted emission with respect to the solution state (Fig. 6).

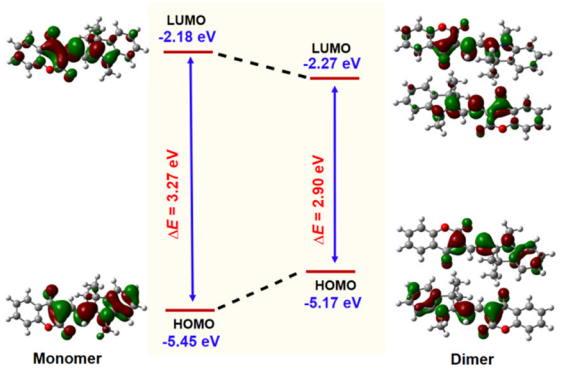

Fig. 6 Energy optimized structure of probe **2** in the monomeric (in solution) and dimeric form (in the solid-state).

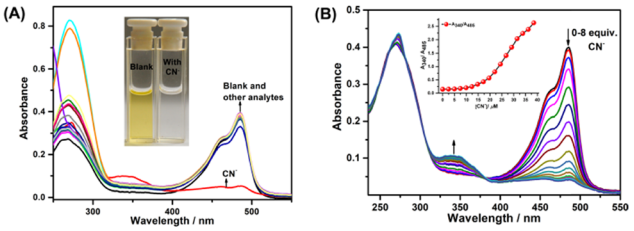

Fig. 7 (A) UV-vis spectra of **2** (5 μM) with various anions and biothiols (7 equiv.). (Inset) Visible colour change of probe **2** upon the addition of CN^-. (B) UV-vis titration of **2** (5 μM) with increasing amount of cyanide (0–35 μM) in acetonitrile solution.

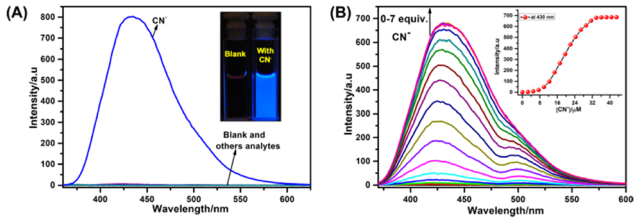

Fig. 8 (A) Fluorescence spectra of **2** (5 μM, λ_{ex} = 340 nm, λ_{em} = 430 nm) with various anions and biothiols (7.0 equiv.). (Inset) Naked eye fluorescence color changes under UV light. Upon the addition of CN^- (B) fluorescence titration of **2** (5 μM) in CH_3CN with increasing amount of cyanide (0–35 μM). (Inset) Plot of fluorescence intensity as a function of cyanide concentration.

Colorimetric and fluorometric CN^- detection

The absorption spectra of probe **2** (5 μM) were measured in acetonitrile solution at 25 °C. As shown in Fig. 7A, the yellow solution containing probe **2** shows a distinctive absorption band at 485 nm, attributed to the typical internal charge transfer (ICT) transition in the probe and supported by an electrochemical study (*vide infra*). Addition of 7.0 equiv. of each respective anion (HS^-, AcO^-, F^-, Cl^-, Br^-, I^-, SO_3^{2-}, SO_4^{2-}, $S_2O_3^{2-}$, CO_3^{2-}, N_3^-, NO_3^-, ClO^-, $H_2PO_4^-$ HSO_4^-, HSO_3^-, HCO_3^-, cysteine (Cys), glutathione (GSH)) to the solution scarcely changes the spectrum. In contrast, as shown by the red line, the addition of cyanide leads to a decrease in the 485 nm band, along with the appearance of a significantly blue-shifted band at 340 nm. A noticeable colour change from yellow to colorless was observed, suggesting that the ICT progress was inhibited by the nucleophilic addition of cyanide to probe **2** (Fig. 7A inset). Fig. 7B shows the results of absorption titration of **2** with CN^-. The gradual addition of CN^- (0–7 equiv.) to the solution leads to a decrease in the 485 nm band, along with an increase in the 340 nm band. In addition, a well-defined isosbestic point was also noted at 392 nm, indicating the formation of the probe **2-CN** adduct.

The fluorescence spectra of **2** in the absence and presence of CN^- were first recorded in acetonitrile solution. The result shows that probe **2** (5 μM) has a very weak fluorescence (ϕ = 0.03) at 503 nm when excited at 340 nm (λ_{max} of UV-vis spectra of probe **2-CN**). The internal charge transfer (ICT) process from the excited state of the 1,3,3-trimethylindoline moiety to electron-deficient chroman-2,4-dione is responsible for the weak fluorescence. After the treatment of CN^- (7 equiv.) with probe **2** (5 μM), a remarkable enhancement in fluorescence intensity (ϕ = 0.60) was observed, indicating the inhibition of ICT. Meanwhile other anions such as HS^-, AcO^-, F^-, Cl^-, Br^-, I^-, SO_3^{2-}, SO_4^{2-}, $S_2O_3^{2-}$, CO_3^{2-}, N_3^-, NO_3^-, ClO^-, $H_2PO_4^-$, HSO_4^-, HSO_3^-, and HCO_3^-, as well as cysteine (Cys) and glutathione (GSH) showed negligible fluorescence change (Fig. 8A). During the fluorescence titration of **2** with increasing amount of CN^- (0–7.0 equiv.), the fluorescence intensity was enhanced by ~2270-fold at 430 nm with a 75 nm blue shift in the acetonitrile solution (Fig. 8B). No further enhancement was observed even after adding more than 7.0 equiv. of cyanide.

Under well-established sensing conditions, the detection limit of probe **2** was calculated to be as low as 0.37 μM (Fig. 9A) from fluorescence titration data in acetonitrile. This specifies that the probe can be used to detect a very low concentration of CN^-. The time-dependent fluorescence responses of probe **2** to cyanide were monitored upon the addition of 7.0 equiv. of CN^- in acetonitrile solution at room temperature (Fig. 9B). The maximum fluorescence of **2** was reached within 3.5 minutes, and no further enhancement was observed afterwards. This observation points to a relatively fast reaction of **2** with CN^-. The Job's plot analysis reveals an inflection point ~0.5, which supports a 1 : 1 stoichiometry between probe **2** and CN^- (Fig. S8†). Moreover, the fluorescence lifetime (τ) of **2** (0.1076 ns), measured in acetonitrile, was increased to 3.102 ns in the presence of 7 equiv. of CN^- (Fig. 9C).

The sensing ability of **2** toward CN^- was also measured in a 50% aqueous acetonitrile solution. Probe **2** showed maximum fluorescence enhancement only in the presence of CN^- at 420 nm, while other anions such as HS^-, AcO^-, F^-, Cl^-, Br^-, I^-, SO_3^{2-}, SO_4^{2-}, $S_2O_3^{2-}$, CO_3^{2-}, N_3^-, NO_3^-, ClO^-, $H_2PO_4^-$, HSO_4^-, HSO_3^-, and HCO_3^-, as well as cysteine (Cys) and glutathione (GSH) did not show fluorescence change except for acetate, which showed negligible fluorescence enhancement (Fig. 10A). During fluorescence titration in 50% aqueous acetonitrile solution, ~172-fold (Fig. 10B) fluorescence intensity enhancement is observed for probe **2** in the presence of 200 equiv. of CN^-. The influence of pH on cyanide sensing by probe **2** (5 μM) was verified in the fluorescence spectroscopic channel. At pH values between 6 and 8, probe **2** showed good sensitivity towards CN^-. However, the physiological pH (7.0) is most suitable for the detection of cyanide (Fig. S9 in the ESI†). It can be assumed that at pH values below 4, the protonation of CN^- decreased the

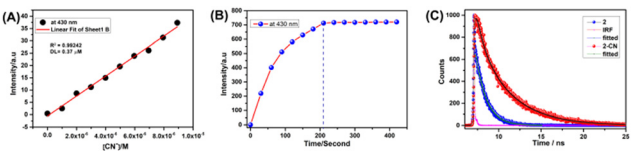

Fig. 9 (A) A calibration curve for CN^- over a concentration range from 0–10 μM derived from fluorescence titration with **2** (5.0 μM). (B) Time course of the fluorescence response of probe **2** to 7 equiv. of CN^- in CH_3CN at 430 nm showing that the reaction completed within 3.5 min. (C) Time resolved fluorescence spectra of **2** (5 μM) before and after the addition of CN^- in CH_3CN.

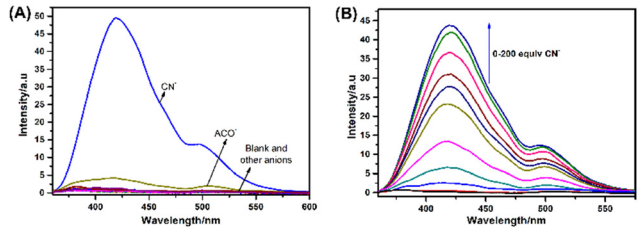

Fig. 10 (A) Fluorescence spectra of **2** (5 μM, λ_{ex} = 340 nm, λ_{em} = 420 nm) with various anions [HS^-, AcO^-, F^-, Cl^-, Br^-, I^-, SO_3^{2-}, SO_4^{2-}, $S_2O_3^{2-}$, CO_3^{2-}, N_3^-, NO_3^-, ClO^-, $H_2PO_4^-$, HSO_4^-, HSO_3^-, HCO_3^-, cysteine (Cys), glutathione (GSH) and CN^- (200 equiv.)] in 50% aqueous CH_3CN solution. (B) Fluorescence titration of **2** (5 μM) in 50% aqueous CH_3CN solution with increasing amount of CN^- solution (0–200 equiv.).

reactivity of cyanide ions in the sample solution and nearly no response was observed.

Mechanistic insight into cyanide binding

The mechanism of the probe–cyanide interaction is shown in Scheme 3. The structure of probe **2** was designed by using a coumarin-derived (chroman-2,4-dione) electron acceptor and the indoline moiety as an electron donor. It is assumed that the nucleophilic addition of CN^- to the polarized C═C bond attached to the indoline group and the internal charge transfer (ICT) from indoline to chroman-2,4-dione is interrupted. In the **2-CN** adduct, the fluorescence of chroman-2,4-dione is recovered through locally excited emission (LE). In addition, the absorption spectra showed noticeable changes of the absorption band at 485 nm, which was shifted to the band at 340 nm and enhanced significantly (Fig. 7B).

To confirm this mechanism, ^{1}H NMR titration with CN^- was carried out in $CDCl_3$ (Fig. 11). As illustrated in Scheme 2, upon the addition of tetra-*n*-butyl ammonium cyanide (TBACN) to **2** (*Z* + *E*), a single isomer of the cyanide adduct is formed. As shown in Fig. 11A and B, the vinylic protons $H_{7,7'}$ and $H_{6,6'}$ and methyl protons $H_{8,8'}$ and $H_{9,9',10,10'}$ of probe **2** at 9.05, 8.82, 8.25, 7.66, 3.67 and 1.79 ppm gradually disappeared upon the addition of cyanide (0–1.25 equiv.) and concurrently, new peaks were generated at δ = 7.42 ($H_{7'}$, J = 16 Hz), 7.12 ($H_{6'}$, J = 16 Hz), 2.76, 1.47 and 1.21 ppm respectively. With the help of ^{1}H–^{1}H COSY NMR of **2-CN** (2 + 1.25 equiv. of CN^-), all the protons were assigned (Fig. S10 and S11†). The very high coupling constant (J = 16 Hz) between $H_{7'}$–$H_{6'}$ confirms the *trans* disposition of the $H_{7'}$–$H_{6'}$ protons which is only possible if CN^- attacks the C═C bond attached to the indoline moiety. Interestingly, here, methyl protons ($H_{9,9',10,10'}$) became magnetically non-equivalent after the addition of CN^- and two sharp singlets at 1.47 and

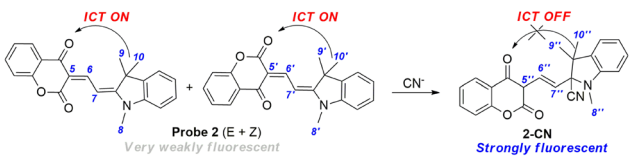

Scheme 3 Plausible mechanism for cyanide binding.

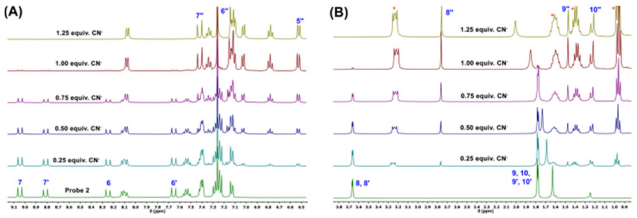

Fig. 11 ^{1}H NMR titration of **2** with CN^- (0–1.25 equiv.) at (A) aromatic and (B) aliphatic region in $CDCl_3$ (* tetrabutylammonium).

1.21 ppm have been generated. Besides, a new signal, $H_{5''}$, was generated at δ = 6.52 ppm in the **2-CN** adduct. These observations clearly indicated that the cyanide anion was added to the polarized C═C bond attached to the indoline moiety and suggested a 1 : 1 reaction between probe **2** and CN^-.

Electrochemical study

In an ICT-based probe, after light absorption, the donor part is oxidized, and the acceptor part is reduced. Therefore, in the cyclic voltammogram, a redox wave was expected for probe **2**. The redox wave for **2** was found irreversible, and the oxidation is assigned to the electron-donating indoline unit, whereas the reduction is assigned to the electron-accepting chroman-2,4-dione moiety. For irreversible oxidation or reduction systems, E(p) (*i.e.*, anodic potentials (E_a) for oxidation or cathodic potentials (E_c) for reduction) is the most frequent choice for representing their electrochemical potentials (Fig. 12). The E_a and E_c are obtained at 1.32 V and −1.42 V, respectively, with a 2.74 volt E_a–E_c separation.

Theoretical study

To gain insight into the electronic transitions and relation between structural and molecular spectral changes of probe **2** and the **2-CN** adduct, geometry optimization and time-dependent DFT (TD-DFT) calculations were carried out in CH_3CN. The geometry-optimized structures of **2** and **2-CN** and the selected calculated molecular orbitals (MOs) are shown in Fig. 13. In Table 1, the computed vertical excitation energies and composition of the related transitions assigned to the experimental UV-vis spectra in CH_3CN and theoretical UV-vis spectra (Fig. S9†) are displayed. The related occupied molecular orbital (HOMO) of probe **2** is located on the whole

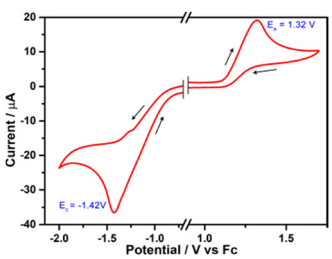

Fig. 12 Cyclic voltammogram of probe **2** in CH_3CN containing 0.1 M tetra-*n*-butyl ammonium perchlorate at 298 K.

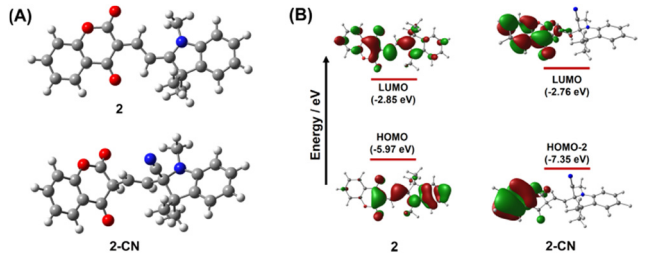

Fig. 13 (A) Energy minimized structures of **2** and **2-CN**. (B) Energy level diagram of **2** and **2-CN** obtained from ground state TD-DFT (B3LYP/6-31G(d,p)) calculation in CH_3CN (isovalue = 0.03).

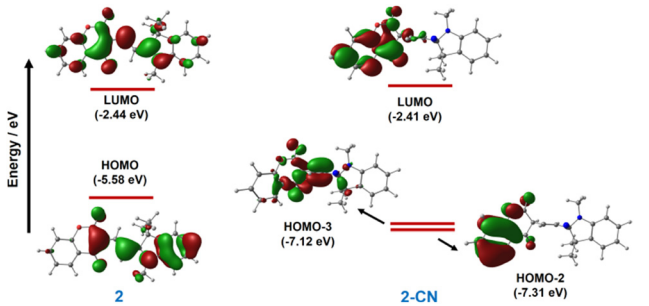

Fig. 14 Energy level diagram of selected molecular orbitals of **2** and **2-CN** adduct, obtained from excited state TD-DFT (B3LYP/6-31G(d,p)) calculation in CH_3CN (isovalue = 0.03).

compound except for the benzene ring of chroman-2,4-dione. In contrast, the lowest unoccupied molecular orbital (LUMO) corresponds to the π* orbital of the entire molecule. The spectral bands in the UV-visible region between 280 and 540 nm are assigned to various charge transfer transitions.

The TDDFT calculations for **2** indicate that the experimental bands at λ_{max} = 485 nm (2.55 eV) originated from strong HOMO → LUMO (444 nm (2.79 eV) f = 1.108) transitions (Table 1) which can be assigned as internal charge transfer from 1,3,3-trimethylindoline to the chroman-2,4-dione moiety. For **2-CN**, the experimental transitions at 340 nm (3.65 eV) are predominantly contributed by HOMO−2 → LUMO (345 nm, f = 0.006 and 316 nm, f = 0.057) (Table 1), which can be assigned as locally excited π–π* transitions. Notably, the chroman-2,4-dione based HOMO and LUMO in **2-CN** are adequately stabilized and destabilized compared to **2**, which designates the blue shifted absorption band in **2-CN**.

The TDDFT calculations at the singlet excited state reveal that the weak emission of probe **2** at 502 nm (2.47 eV) is due to the internal charge transfer (ICT), assigned as a HOMO → LUMO transition at 435 nm (2.85 eV) (Fig. 14). In the **2-CN** adduct, the internal charge transfer (ICT) from 1,3,3-trimethylindoline to chroman-2,4-dione is restricted, and the experimental very strong blue emission band at ~431 nm (3.64 eV) arises from the locally excited (LE) chroman-2,4-dione moiety, characterized as HOMO−2, and HOMO−3 to LUMO transition at 346 nm (Table 2 and Fig. 14).

Real-time detection of cyanide using paper strip

Probe **2** was used to prepare a solid-state sensor kit by drop casting on a strip of filter paper from its acetonitrile solution (100 mM). The test paper strip was dipped in tetra-*n*-butyl ammonium cyanide solution at various concentrations and dried. When the concentration of cyanide solution was increased gradually, the dry paper strip under UV light at 365 nm showed orange yellow to intense green fluorescence (Fig. 15A). In the solution phase cyanide detection, after treatment with cyanide, probe **2** showed bright blue fluorescence (*vide supra*). In contrast to the solution phase detection of cyanide, green fluorescence is observed here. The compound has AIE property, and it shows red-shifted emission at high concentration and in the solid state. Here compound **2** loaded dry paper strip was used; therefore, red-shifted green emission instead of blue was observed after CN addition (Fig. 15A). This phenomenon supported the dual-state emission character of the **2-CN** adduct. For further investigation, tetra-*n*-butyl ammonium cyanide solution was added to the solid crystal of probe **2**. An immediate colour change was observed from bright red to intense blue (Fig. 15B). As in the paper strip CN detection, the compound concentration is comparatively higher (100 μM) than the solution phase (5 μM) CN detection, and the green emission of the paper strip is due to the aggregated **2-CN** adduct formation. To support this, PL titration with CN ions at a higher concentration of probe **2** (100 μM) was performed. The weakly emissive probe **2** (100 μM) showed dual emission with a λ_{em} at 520 nm and 405 nm upon adding 0.25–1 equiv. of CN ion and green luminescence is clearly visible under a laboratory handheld UV lamp (365 nm) (Fig. 16). Further, the dual emission disappeared, and a broad emission with a λ_{em} at 430 nm was observed upon the addition of cyanide (2–3 equiv.) (Fig. 16A). The compound **2**-loaded paper strips display a clear fluorescence change upon exposure to a low cyanide concentration (10 μM). Thus, the portable test paper kit can be used for the visual detection of cyanide.

Table 1 Selected ground state transitions for **2** and **2-CN** in CH_3CN, obtained from TD-DFT calculation at B3LYP/6-31G(d,p)

Compound	Wavelength (nm eV^{-1})		Transitions	Oscillator strength (f)	Contribution (CI)
	Experimentally observed	Theoretically obtained			
2	485 nm (2.55 eV)	444 nm (2.79 eV)	HOMO → LUMO	1.108	0.75
2-CN	340 nm (3.65 eV)	345 nm (3.59 eV)	HOMO−2 → LUMO	0.057	0.63
		316 nm (3.92 eV)	HOMO−2 → LUMO	0.006	0.67

Table 2 Selected TD-DFT transitions of the singlet excited state of probe **2** and the **2-CN** adduct, calculated in CH_3CN

Compound	Wavelength (nm eV^{-1}) Experimentally observed	Theoretically obtained	Transition	Oscillator strength (f)	Contribution (CI)
2	502 nm (2.47 eV)	435 nm (2.85 eV)	HOMO → LUMO	1.106	0.70
2-CN	431 nm (3.64 eV)	346.0 nm (3.58 eV)	HOMO−3 → LUMO	0.0043	0.63
			HOMO−2 → LUMO		0.15

Conclusions

In conclusion, a new 1,3,3-trimethylindoline and chroman-2,4-dione conjugate, **2**, was synthesized in two steps. Probe **2** was characterized by several spectroscopic techniques and single-crystal X-ray diffraction. The dual state emission (DSE) property of probe **2** showed bright fluorescence emissions both in concentrated solution and in the solid state. It emits bright-green fluorescence in CH_3CN, whereas in the solid state, it exhibits intense orange-red fluorescence under UV-light illumination. In the fluorescence channel, the probe rapidly detects cyanide by fluorescence light-up through the restriction of ICT. The time-dependent fluorescence study reveals that the cyanide addition reaction with the probe has been completed within 3.5 minutes. The calculated detection limits suggested that the probe can detect CN^- at the sub-micromolar level. The probe exhibits stronger selectivity and affinity towards cyanide than its likely competitors. This detection mechanism was confirmed by the ^{1}H NMR titration study. A solid-state paper strip, coated with probe **2**, has been employed for practical applications to detect a different concentration of cyanide.

Experimental section

Materials and physical measurements

All the chemicals used for synthesis and sensing studies were purchased from commercial suppliers (Aldrich, Alfa Aesar and Spectrochem India) and used as received without further purification. All 1D and 2D NMR spectra were recorded on a Bruker AVANCE II (400 MHz) spectrometer, and chemical shifts were expressed in ppm using residual protic solvent as the internal standard. High-resolution mass spectrometry (HRMS) data for all the synthesized compounds were collected on a Waters XeVo G2-XS QTof mass spectrometer connected to the ACQUITY UPLC I-Class System *via* an electrospray ionization (ESI) interface. All the NMR and ESI-HRMS data were processed in MestReNova V12.0.0-20080. Infrared spectra were recorded using a PerkinElmer FT-IR spectrometer with KBr pellets in the range of 4000–400 cm^{-1}. Elemental analysis was done using a PerkinElmer 2500 series II elemental analyzer. UV-vis spectra were recorded on a Carry 60 UV-vis spectrophotometer (Agilent Technologies), whereas PL spectra were recorded on a PerkinElmer LS55 fluorescence spectrophotometer with a quartz cuvette (path length = 1 cm). The luminescence lifetime measurements were carried out on a time-correlated single-photon counting (TCSPC) picosecond spectrophotometer (LifeSpec-II, Edinburgh Instruments, U.K.). A Malvern Zen 3690 instrument has been used for dynamic light scattering (DLS) measurements. Transmission electron microscopy (TEM) analysis was carried out using a JEOL JSM 100CX with an accelerating voltage of 200 kV.

Synthesis of 4-chloro-3-formylcoumarin (1)

4-Hydroxycoumarin (2.43 g, 15.0 mmol) was dissolved in 12 mL of DMF and 4.18 mL of $POCl_3$ was added to the solution dropwise at 0 °C. Then, the mixture was stirred at 55 °C for 2 hours. After that, the reaction mixture was cooled down to room temperature and was poured into 50 ml ice-cold water with vigorous stirring. A yellow precipitate was observed and kept overnight at 0 °C. The precipitate was collected by filtration, washed with diethyl ether and dried under vacuum. The product was recrystallized from acetone, and plate-like crystalline compounds were isolated with good yield. Yield 78% (2.72 g). FTIR in KBr disk (ν/cm^{-1}): 3434, 3006, 1608, 1573, 1496, 1327, 1217, 757. MS (HRMS; positive mode): (m/z, %): 208.9984 [$(C_{10}H_5ClO_3 + H)^+$, 100%]; calcd. m/z, 208.9927; ^{1}H-NMR (400 MHz, $CDCl_3$): δ (ppm) = 10.38 (s, 1H), 8.13 (d, J = 8 Hz, 1H), 7.74 (d, J = 8 Hz, 1H), 7.47–7.39 (m, 2H). ^{13}C NMR (100 MHz, $CDCl_3$): δ (ppm) = 187.0, 158.6, 153.7, 153.4, 135.9, 127.8, 125.7, 118.5, 118.3, 117.3.

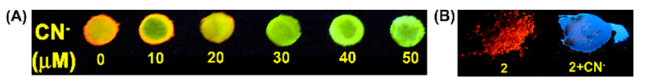

Fig. 15 (A) Fluorescence response of probe **2** immobilized paper strips upon exposure to various concentrations of cyanide (0–50 μM). (B) Digital photograph of solid probe **2** and instantly formed **2-CN** after cyanide addition.

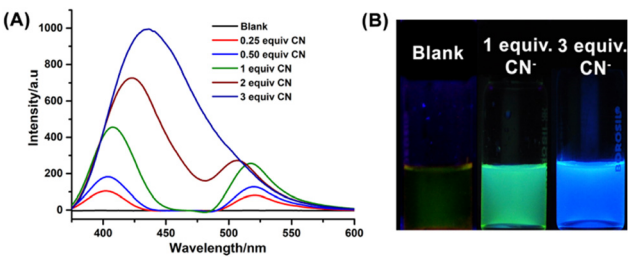

Fig. 16 (A) Fluorescence titration of **2** (100 μM, λ_{ex} = 340 nm) with increasing amount of cyanide (0–3 equiv.) in acetonitrile. (B) Naked eye fluorescence colour changes upon the addition of CN^- under UV light (365 nm).

Synthesis of (*E*)-3-((*E*)-2-(1,3,3-trimethylindolin-2-ylidene) ethylidene)chroman-2,4-dione/(*Z*)-3-((*E*)-2-(1,3,3-trimethylindolin-2-ylidene)ethylidene)chroman-2,4-dione (1 : 1) (2)

4-Chloro-3-formylcoumarin (**1**) (0.208 g, 1.00 mmol) and 1,2,3,3-tetramethyl-3*H*-indolium iodide (0.301 g, 1.00 mmol) were dissolved in 10 ml distilled ethanol, and 200 μL of triethyl amine was added to it. An immediate colour change was observed from brown to deep green, and the reaction mixture was refluxed for 12 h under N_2. A reddish residue was obtained after the completion of reaction. The precipitate was collected by filtration and then washed with distilled ethanol (30 ml × 3), and a dark red solid was isolated and dried under vacuum. Yield 74% (269 mg). Anal. calcd. for $C_{22}H_{19}NO_3$ (MW = 345.39): C, 76.50; H, 5.54; N, 4.06; found: C, 76.54; H, 5.57; N, 4.09; FTIR in KBr disk (ν/cm^{-1}): 3674, 1703, 1622, 1520, 1339, 1263, 1228, 862. MS (HRMS; positive mode): (*m*/*z*, %): 346.1399 [($C_{22}H_{19}NO_3$ + H^+), 100%]; calcd. *m*/*z*, 346.1365; ^{1}H-NMR (400 MHz, $CDCl_3$): δ (ppm) = 9.05 (d, J = 14.8 Hz 1H, H_7), 8.82 (d, J = 14.8 Hz 1H, $H_{7'}$), 8.25 (d, J = 14.8 Hz, 1H, H_6), 8.11 (t, J = 8 Hz, 2H, $H_{13,13'}$), 7.66 (d, J = 14.8 Hz, 1H, $H_{6'}$), 7.57–7.51 (m, 2H, $H_{4,4'}$), 7.42–7.38 (m, 4H, $H_{2,2',3,3'}$), 7.29–7.22 (m, 6H, $H_{11,11',12,12',14,14'}$), 7.13 (d, J = 8 Hz, 2H, $H_{1,1'}$), 3.67–3.66 (m, 6H, $H_{8,8'}$), 1.79–1.78 (m, 12H, $H_{9,9',10,10'}$). ^{13}C NMR (100 MHz, $CDCl_3$): δ (ppm) = 180.4, 179.6, 179.4, 179.1, 165.5, 163.1, 155.1, 154.5, 153.9 (2C), 153.0 (2C), 142.5 (2C), 141.5, 141.4, 134.1, 133.7, 128.7, 128.6, 126.7, 126.3, 125.6 (2C), 123.8, 123.7, 122.4 (2C), 122.2, 121.0, 117.1 (2C), 110.6, 110.5, 107.2, 106.8, 101.6, 101.0, 49.7, 31.5, 31.1, 28.9 (3C).

Data availability

The details of general experimental procedures, single crystal analysis, structural characterization, optical spectra, additional NMR and HRMS spectra, *etc.* supporting this article are available in the ESI† as provided.

Author contributions

Snehadrinarayan Khatua: conceptualization, formal analysis, funding acquisition, supervision, visualization, writing – original draft, writing – review & editing. Sumit Kumar Patra: conceptualization, data collection, investigation, visualization, writing – original draft. Monosh Rabha: data collection Deikrisha Lyngdoh Lyngkhoi: data collection, formal analysis, writing – review & editing. Jogat Gogoi: data collection, formal analysis, writing – review & editing. Bhaskar Sen: formal analysis, investigation.

Conflicts of interest

There are no conflicts to declare.

Acknowledgements

This work was financially supported by DST, India (No. SB/FT/CS/115/2012). We thank the DST Purse program for use of the single-crystal X-ray diffraction facility at NEHU and Sophisticated Analytical and Instrumentation Facility (SAIF), North-Eastern Hill University for the NMR and ESI-MS data. S. K. P. and B. S. thank CSIR, India for the senior research fellowship (SRF). Dr. Susnata Pramanik (SRM Institute of Science & Technology, Chennai) is acknowledged for useful discussions. We also thank the DST-FIST program (No. SR/FST/CS-II/2019/99(C)), Govt. of India for providing the HRMS instrument to the Dept. of Chemistry, NEHU, Shillong.

Notes and references

1 O. Ostroverkhova, *Chem. Rev.*, 2016, **116**, 13279–13412.
2 E. H. Kim, G. Chin, G. Rong, K. E. Poskanzer and H. A. Clark, *Acc. Chem. Res.*, 2018, **51**, 1023–1032.
3 T. P. I. Saragi, T. Spehr, A. Siebert, T. Fuhrmann-Lieker and J. Salbeck, *Chem. Rev.*, 2007, **107**, 1011–1065.
4 Z. Yang, X. Fan, X. Liu, Y. Chu, Z. Zhang, Y. Hu, H. Lin, Y. Qian and J. Hua, *Chem. Commun.*, 2021, **57**, 3099–3102.
5 J. Luo, Z. Xie, J. W. Y. Lam, L. Cheng, H. Chen, C. Qiu, H. S. Kwok, X. Zhan, Y. Liu, D. Zhu and B. Z. Tang, *Chem. Commun.*, 2001, 1740–1741.
6 M. Kaur, H. Kaur, M. Kumar and V. Bhalla, *Chem. Rec.*, 2021, **21**, 240–256.
7 F. Khan, A. Ekbote, S. M. Mobin and R. Misra, *J. Org. Chem.*, 2021, **86**, 1560–1574.
8 J. Mei, N. L. C. Leung, R. T. K. Kwok, J. W. Y. Lam and B. Z. Tang, *Chem. Rev.*, 2015, **115**, 11718–11940.
9 X. Cai and B. Liu, *Angew. Chem., Int. Ed.*, 2020, **59**, 9868–9886.
10 R. Misra, T. Jadhav, B. Dhokale and S. M. Mobin, *Chem. Commun.*, 2014, **50**(65), 9076–9078.
11 Z. Guo, C. Yan and W.-H. Zhu, *Angew. Chem., Int. Ed.*, 2020, **59**, 9812–9825.
12 J. L. Belmonte-Vázquez, Y. A. Amador-Sánchez, L. A. Rodríguez-Cortés and B. Rodríguez-Molina, *Chem. Mater.*, 2021, **33**, 7160–7184.
13 H. Wu and C. Tong, *Anal. Chem.*, 2020, **92**, 8859–8866.
14 Y. Zhang, Y. Yan, S. Xia, S. Wan, T. E. Steenwinkel, J. Medford, E. Durocher, R. L. Luck, T. Werner and H. Liu, *ACS Appl. Mater. Interfaces*, 2020, **12**, 20172–20179.
15 Q. Qiu, P. Xu, Y. Zhu, J. Yu, M. Wei, W. Xi, H. Feng, J. Chen and Z. Qian, *Chem. – Eur. J.*, 2019, **25**, 15983–15987.
16 T. Stoerkler, G. Ulrich, A. D. Laurent, D. Jacquemin and J. Massue, *J. Org. Chem.*, 2023, **88**(13), 9225–9236.
17 D. Xi, Y. Xu, R. Xu, Z. Wang, D. Liu, Q. Shen, L. Yue, D. Dang and L. A. Meng, *Chem. – Eur. J.*, 2020, **26**, 2741–2748.
18 X. Zhang, Y. Zhou, M. Wang, Y. Chen, Y. Zhou, W. Gao, M. Liu, X. Huang and H. Wu, *Chem. – Asian J.*, 2020, **15**, 1692–1700.
19 Y. J. Yang, M. Dai, Y. J. Reo, C. W. Song, S. Sarkar and K. H. Ahn, *Anal. Chem.*, 2021, **93**, 7523–7531.
20 N. S. Kumar, M. D. Gujrati and J. N. Wilson, *Chem. Commun.*, 2010, **46**, 5464–5466.
21 P. Gopikrishna and P. K. Iyer, *J. Phys. Chem. C*, 2016, **120**, 26556–26568.
22 Y. Xu, L. Ren, D. Dang, Y. Zhi, X. Wang and L. Meng, *Chem. – Eur. J.*, 2018, **24**, 10383–10389.

23 Q. Shao, K. Liang, H. Ling, Y. Wang, Z. Yan, G. Xia and H. Wang, *J. Mater. Chem. C*, 2020, **8**, 4549–4556.
24 H. Wu, Z. Chen, W. Chi, A. K. Bindra, L. Gu, C. Qian, B. Wu, B. Yue, G. Liu, G. Yang, L. Zhu and Y. Zhao, *Angew. Chem., Int. Ed.*, 2019, **58**, 11419–11423.
25 W. Fang, K. Liu, G. Wang, Y. Liang, R. Huang, T. Liu, L. Ding, J. Peng, H. Peng and Y. Fang, *Anal. Chem.*, 2021, **93**(24), 8501–8507.
26 S. Kumar, P. Singh, P. Kumar, R. Srivastava, S. K. Pal and S. Ghosh, *J. Phys. Chem. C*, 2016, **120**, 12723–12733.
27 V. D. Singh, A. K. Kushwaha and R. S. Singh, *Dyes Pigm.*, 2021, **187**, 109117.
28 Y. Qi, G. Wang, Z. Ge, Y. Liu, Y. Yu and M. Xue, *J. Mater. Chem. C*, 2017, **5**, 11030–11038.
29 B. Muthuraj, S. Mukherjee, C. R. Patra and P. K. Iyer, *ACS Appl. Mater. Interfaces*, 2016, **8**, 32220–32229.
30 Y. X. Lei, W. B. Dai, Z. Q. Liu, S. Guo, Z. X. Cai, J. B. Shi, X. Y. Zheng, J. G. Zhi, B. Tong and Y. P. Dong, *Mater. Chem. Front.*, 2019, **3**, 284–291.
31 D. K. Singh, K. Jang, J. Kim, J. Lee and I. Kim, *ACS Comb. Sci.*, 2019, **21**, 408–416.
32 Y. Li, Y. Lei, L. Dong, L. Zhang, J. Zhi, J. Shi, B. Tong and Y. Dong, *Chem. – Eur. J.*, 2019, **25**, 573–581.
33 S. Guo, Y. Zhang, J. Huang, L. Kong and J. Yang, *CrystEngComm*, 2021, **23**, 221–226.
34 S. Guo, G. Zhang, L. Kong, Y. Tian and J. Yang, *Chem. – Eur. J.*, 2020, **26**, 3834–3842.
35 Y. Lei, Q. Liu, L. Dong, Z. Cai, J. Shi, J. Zhi, B. Tong and Y. Dong, *Chem. – Eur. J.*, 2018, **24**, 14269–14274.
36 Z. Xiang, Z.-Y. Wang, T.-B. Ren, W. Xu, Y.-P. Liu, X.-X. Zhang, P. Wu, L. Yuan and X.-B. Zhang, *Chem. Commun.*, 2019, **55**, 11462–11465.
37 S. Yokoyama and N. Nishiwaki, *J. Org. Chem.*, 2019, **84**, 1192–1200.
38 W. Xi, J. Yu, M. Wei, Q. Qiu, P. Xu, Z. Qian and H. Feng, *Chem. – Eur. J.*, 2020, **26**, 1–6.
39 H. Liu, S. Zhang, L. Ding and Y. Fang, *Chem. Commun.*, 2021, **57**, 4011–4014.
40 R. Kaushik, A. Ghosh, A. Singh, P. Gupta, A. Mittal and D. Jose, *ACS Sens.*, 2016, **1**, 1265–1271.
41 I. Bhowmick, D. J. Boston, R. F. Higgins, C. M. Klug, M. P. Shores and T. Gupta, *Sens. Actuators, B*, 2016, **235**, 325–329.
42 J. K. Fawell, *Guidelines for Drinking-water Quality*, World Health Organization, Geneva, 2nd edn, vol. 2, 1996.
43 S. I. Baskin, J. B. Kelly, B. I. Maliner, G. A. Rockwood and C. K. Zoltani, *Medical Aspects of Chemical and Biological Warfare*, TMM Publication, Washington, 2008, ch. 11, pp. 371–410.
44 S. Khatua, D. Samanta, J. W. Bats and M. Schmittel, *Inorg. Chem.*, 2012, **51**, 7075–7086.
45 M. J. Li, Z. H. Lin, X. D. Chen and G. N. Chen, *Dalton Trans.*, 2014, **43**, 11745–11751.
46 K. S. Bejoymohandas, A. Kumar, S. Sreenadh, E. Varathan, S. Varughese, V. Subramanian and M. L. P. Reddy, *Inorg. Chem.*, 2016, **55**, 3448–3461.
47 S. K. Patra, S. K. Sheet, B. Sen, K. Aguan, D. R. Roy and S. Khatua, *J. Org. Chem.*, 2017, **82**, 10234–10246.
48 Z. Xu, X. Chen, H. N. Kim and J. Yoon, *Chem. Soc. Rev.*, 2010, **39**, 127–137.
49 A. K. Mahapatra, K. Maiti, S. K. Manna, R. Maji, C. Das Mukhopadhyay, B. Pakhira and S. Sarkar, *Chem. – Asian J.*, 2014, **9**, 3623–3632.
50 I. J. Kim, M. Ramalingam and Y. A. Son, *Sens. Actuators, B*, 2017, **246**, 319–326.
51 J. Oh, I. Jeon, D. Kim, Y. You, D. Baek, S. J. Kang and J. Lee, *ACS Appl. Mater. Interfaces*, 2020, **12**, 4934–4943.
52 A. Mondal, S. Nag and P. Banerjee, *Dalton Trans.*, 2021, **50**, 429–451.
53 S. Mondal, S. S. Ali, S. Manna, K. Maiti, Md. R. Uddin, S. Mandal, D. Mandal and A. K. Mahapatra, *New J. Chem.*, 2017, **41**, 12581–12588.
54 V. N. Khose, M. Hasan, S. C. Khot, S. M. Mobin, V. Borovkov and A. V. Karnik, *J. Org. Chem.*, 2020, **85**, 1847–1860.
55 C. Gouda, D. Barik, C. Maitra, K.-C. Liang, F.-C. Ho, V. Srinivasadesikan, S. Chandran, S.-P. Wu, M.-C. Lin and H.-C. Lin, *J. Mater. Chem. C*, 2021, **9**, 2321–2333.
56 F.-C. Ho, Y.-J. Huang, C.-C. Weng, C.-H. Wu, Y.-K. Li, J. I. Wu and H.-C. Lin, *ACS Appl. Mater. Interfaces*, 2020, **12**, 53257–53273.
57 D. Wang, H. Li, S. Sun and Y. Xu, *Org. Lett.*, 2020, **22**, 3361–3366.
58 A. Tigreros, J. Zapata-Rivera and J. Portilla, *ACS Sustainable Chem. Eng.*, 2021, **9**, 12058–12069.
59 D. Srikun, E. W. Miller, D. W. Domaille and C. J. Chang, *J. Am. Chem. Soc.*, 2008, **130**, 4596–4597.
60 X. J. He, C. C. Xu, W. Xiong, Y. Qian, J. Y. Fan, F. Ding, H. Deng, H. Chen and J. L. Shen, *Analyst*, 2020, **145**, 29–33.
61 S. D. Padghan, L.-C. Wang, W.-C. Lin, J.-W. Hu, W.-C. Liu and K.-Y. Chen, *ACS Omega*, 2021, **6**, 5287–5296.
62 S. Majeed, M. T. Waseem, H. M. Junaid, G. S. Khan, S. Nawazish, T. Mahmood, A. M. Khan and S. A. Shahzad, *RSC Adv.*, 2022, **12**, 18897–18910.
63 S. D. Padghan, J.-W. Hu, L.-C. Wang, F.-Y. Wang and K.-Y. Chen, *Chem. – Asian J.*, 2023, **18**, e202201293–e202201301.
64 R. Manivannan and Y.-A. Son, *Dyes Pigm.*, 2023, **210**, 110941–110951.
65 X. Peng, J. Du, J. Fan, J. Wang, Y. Wu, J. Zhao, S. Sun and T. Xu, *J. Am. Chem. Soc.*, 2007, **129**, 1500–1501.
66 M. Fu, K. Wang, Q. Ma, J. Zhu, M. Bian and Q. Zhu, *Org. Biomol. Chem.*, 2022, **20**, 672–677.
67 V. F. Traven, V. S. Miroshnikov, T. A. Chibisova, V. A. Barachevsky, O. V. Venidiktova and Yu. P. Strokach, *Russ. Chem. Bull. Int. Ed.*, 2005, **54**, 2417–2424.